JACS
JOURNAL OF THE AMERICAN CHEMICAL SOCIETY

Article

pubs.acs.org/JACS

Unraveling Surface Plasmon Decay in Core–Shell Nanostructures toward Broadband Light-Driven Catalytic Organic Synthesis

Hao Huang,[†,∥] Lei Zhang,[†,∥] Zhiheng Lv,[†] Ran Long,[†] Chao Zhang,[‡] Yue Lin,[†] Kecheng Wei,[†] Chengming Wang,[†] Lu Chen,[†] Zhi-Yuan Li,[‡,§] Qun Zhang,*[,†] Yi Luo,[†] and Yujie Xiong*[,†]

[†]Hefei National Laboratory for Physical Sciences at the Microscale, *i*ChEM (Collaborative Innovation Center of Chemistry for Energy Materials), School of Chemistry and Materials Science, Hefei Science Center (CAS), Synergetic Innovation Center of Quantum Information & Quantum Physics, and National Synchrotron Radiation Laboratory, University of Science and Technology of China, Hefei, Anhui 230026, People's Republic of China

[‡]Beijing National Laboratory for Condensed Matter Physics, Institute of Physics, Chinese Academy of Sciences, Beijing 100190, People's Republic of China

[§]College of Physics and Optoelectronics, South China University of Technology, Guangzhou, Guangdong 510641, China

Supporting Information

ABSTRACT: Harnessing surface plasmon of metal nanostructures to promote catalytic organic synthesis holds great promise in solar-to-chemical energy conversion. High conversion efficiency relies not only on broadening the absorption spectrum but on coupling the harvested energy into chemical reactions. Such coupling undergoes hot-electron transfer and photothermal conversion during the decay of surface plasmon; however, the two plasmonic effects are unfortunately entangled, making their individual roles still under debate. Here, we report that in a model system of bimetallic Au–Pd core–shell nanostructures the two effects can be disentangled through tailoring the shell thickness at atomic-level precision. As demonstrated by our ultrafast absorption spectroscopy characterizations, the achieved tunability of the two effects in a model reaction of Pd-catalyzed organic hydrogenation offers a knob for enhancing energy coupling. In addition, the two intrinsic plasmonic modes at 400–700 and 700–1000 nm in the bar-shaped nanostructures allow for utilizing photons to a large extent in full solar spectrum. This work establishes a paradigmatic guidance toward designing plasmonic–catalytic nanomaterials for enhanced solar-to-chemical energy conversion.

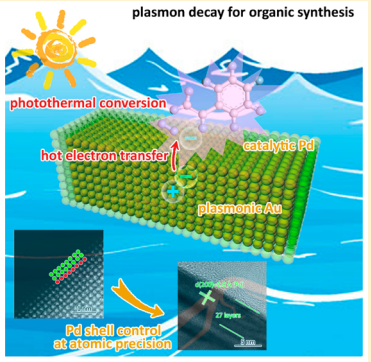

INTRODUCTION

To address the energy crisis, tremendous efforts have been made on the conversion and storage of solar energy in the past decade. Sunlight-driven catalytic organic synthesis, which can convert and store solar energy into the chemical bonds of product molecules, provides an alternative approach to solar energy technologies.[1−12] This approach also opens the possibility of substituting light-driven reactions for conventional thermal-based chemical manufacturing. To fully utilize solar energy for chemical production, one has to achieve two ultimate goals via materials design: robust harvesting of solar light in broad spectrum, particularly in the visible and near-infrared (NIR) regions that account for most of the sunlight photons, and effective coupling of the harvested photons into chemical reactions.

The surface plasmon of metal nanostructures, which can strongly interact with the electromagnetic radiation of incident light, provides an efficient way to couple photon energy onto solid surface.[13] When catalytic sites are integrated near the nanostructure surface, the plasmon-coupled energy may induce chemical transformations in the reactants adsorbed on the sites during plasmon decay.[1] As metals are active catalysts for a wide range of chemical reactions, one can rationally select a metal material (e.g., Pd) as catalytic sites for each specific reaction according to the understanding from previous catalysis studies and readily integrate it with a plasmonic component (e.g., Au) through designing and fabricating heterojunctions or alloys.[1−12] In this scheme, chemical transformations mainly harvest energy from the plasmon decay following the creation of energetic charge carriers (i.e., electron–hole pairs).[14] Specifically, the reactions can be modified or even altered by the plasmon decay through two routes: local heating by converting the carrier energy into the nanoparticle phonon modes[1−6] and direct transfer of the energetic charge carriers to the adsorbed reactants.[7−12] Given the short time scales of electron–phonon scattering and charge recombination,[14] the parameters of heterojunction nanostructures should be precisely controlled so as to maneuver photothermal conversion and hot-electron transfer during the plasmon decay. In other words, the nanostructure design provides an opportunity for synergistically optimizing the two effects on chemical transformations toward

Received: March 9, 2016
Published: May 13, 2016

DOI: 10.1021/jacs.6b02532
J. Am. Chem. Soc. 2016, 138, 6822–6828

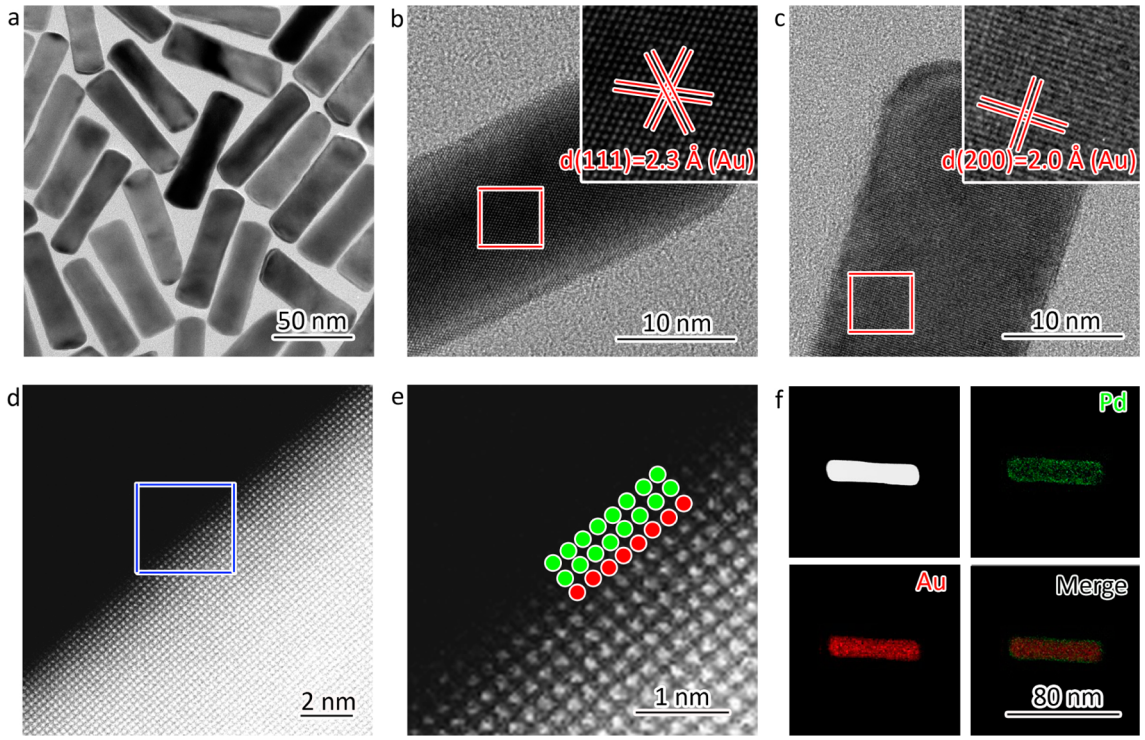

Figure 1. Structural and compositional analyses on Au NRs−Pd_{2L} core−shell nanostructures. (a) TEM image, (b) HRTEM image recorded along [110] orientation, (c) HRTEM image recorded along [001] orientation, (d) HAADF-STEM image, (e) atomic-resolution image taken from the edge region marked by the box in panel d, and (f) STEM and EDS mapping profiles of a single nanostructure: Pd (green) and Au (red).

maximizing the plasmonic−catalytic efficiency. However, the conversion between hot electrons and phonon modes makes the effects entangled in most material and reaction systems, forming the obstacle for understanding the structure−plasmon−catalysis interplay.

Herein, we demonstrate that the effects of photothermal local heating and hot-electron transfer on catalytic reactions can be controlled by tailoring the Pd shell thickness of bar-shaped Au−Pd core−shell nanostructures at atomic-level precision. We select the bar-like shape as the geometry of plasmonic nanostructures on the basis of the fact that the two intrinsic plasmonic bands, transversal mode (T mode) and longitudinal mode (L mode), are located in the visible and NIR regions, respectively, enabling broad-spectrum light harvesting. More importantly, the shell thickness would serve as a knob for maneuvering the processes of hot-electron transfer and local heat generation during surface plasmon decay, setting up a platform for decoding their roles in catalytic reactions. To distinctly differentiate photothermal effect from hot-electron transfer, we adopt the well-studied hydrogenation of styrene as a model reaction to assess plasmonic−catalytic performance under illumination, considering that plasmonic hot electrons have been recognized as detrimental to hydrogenation.[5] Through a precise tuning of the Pd shell thickness to 14 atomic layers, we accomplish the efficiency maximization by taking advantage of local photothermal heating while suppressing the side effect from plasmonic hot electrons. Consequently, under light irradiation of 100 mW cm^{-2} in ambient environment, the yield of styrene hydrogenation into ethylbenzene reaches 76%, an impressive performance comparable to that achieved in the thermally driven process at 80 °C, surpassing the yield of 36% in the dark with a more than 2-fold enhancement.

EXPERIMENTAL SECTION

Synthesis of Au Nanorods (NRs)−Pd Core−Shell Nanostructures. In a typical synthetic procedure for Au NRs−Pd_{7L} core−shell nanostructures, suspension of Au NRs (0.5 mL, 1 mg mL^{-1}) was mixed with an aqueous solution of CTAB (8.85 mL, 0.1 M), followed by the addition of K_2PdCl_4 (250 μL, 0.01 M) and HCl (100 μL, 1 M) aqueous solutions. Subsequently, aqueous solution of ascorbic acid (AA) (100 μL, 0.1 M) was added into the mixture, which was then shaken and kept in an oil bath at 50 °C for 2 h. The color of the mixture turned from brown to black. Finally, the products were centrifuged three times at 8000 rpm for 10 min. The other Au NRs−Pd core−shell nanostructures were synthesized by following a similar procedure except for the use of different amounts of K_2PdCl_4 and AA (50 μL of K_2PdCl_4 and 20 μL of AA for Au NRs−Pd_{2L}, 500 μL of K_2PdCl_4 and 200 μL of AA for Au NRs−Pd_{14L}, and 1000 μL of K_2PdCl_4 and 400 μL of AA for Au NRs−Pd_{27L}, respectively). Here, the 2L, 14L, and 27L denote the numbers of Pd layers in the shells.

Measurements of Catalytic Styrene Hydrogenation. The hydrogenation of styrene was carried out in an 18 cm-tall quartz tube. Au NRs−Pd core−shell nanostructures containing 0.145 mg of Au (based on ICP-MS measurements) were added into the tube, followed by the addition of 0.2 mmol of styrene. Deionized water was added into the solution until the total volume of mixture reached 1 mL. A balloon filled with 100% H_2 was used to enclose the system and provide reaction gas H_2. After exhausting air with H_2, the catalytic reactions were carried out at room temperature under light irradiation. The light irradiation was carried out using a Xe lamp (Solaredge 700, China) at 100 mW cm^{-2}. The experiments under irradiation of $400 < \lambda < 700$ nm and $\lambda > 700$ nm or with thermostatic control were performed under the same conditions by applying different wave-pass cutoff filters or using a homemade thermostatic control device at 20 ± 1 °C, respectively. After the irradiation, Au NRs−Pd catalysts were removed by filtration, and the resulting solution was analyzed by a gas chromatography−mass spectrometry (GC−MS, 7890A and 5975C, Agilent). The thermally driven reactions were performed at certain temperatures by excluding light from the environment with an aluminum foil.

DOI: 10.1021/jacs.6b02532
J. Am. Chem. Soc. 2016, 138, 6822−6828

Ultrafast Spectroscopy Characterization. The femtosecond transient absorption data were recorded on a modified pump−probe spectrometer (ExciPro, CDP) in combination with an ultrafast amplified laser system (Coherent). All of the measurements were performed under ambient conditions, and the samples were dispersed in water. The sample cell was mounted on a rapidly rotating stage (5000 rpm) so as to ensure that the photoexcited volume of the sample was kept fresh during the course of the measurements. The strong pump laser (pulse duration ∼100 fs; pulse energy ∼10 μJ at the sample cell) with a center wavelength at 480 nm (650 nm) was used to examine the T mode (L mode). The weak probe pulses (<1 μJ/pulse at the sample cell) were provided by a stable white-light continuum. The time delays between the pump and probe pulses were varied by a motorized optical delay line (minimum step, 1.56 fs; maximum delay, ∼3.0 ns). The spectral and temporal profiles of the pump-induced transient absorbance changes were visualized by a 1024-pixel imaging spectrometer (CDP2022i) and further processed by an ExiPro 2.6 software.

DDA Calculations. DDA is a computational method developed for investigating both the scattering and the absorption of electromagnetic radiation by particles with sizes on the order of or smaller than the wavelength of incident light. In the calculations, the particle is divided into an array of N polarizable point dipoles, each of which is characterized by a polarizability of α_i. When the system is excited by a monochromatic incident plane wave E_{inc}, each dipole of the system will be subjected to an electric field that can be split into two contributions: (i) the incident radiation field $E_{i,inc}$ and (ii) the field radiated by all of the other induced dipoles $E_{i,dip}$. The sum of both fields is the so-called local field at each dipole ($E_{i,loc} = E_{i,inc} + E_{i,dip}$). Each dipole can be expressed as an oscillating polarization with the dipole moment being $P_i = \alpha_i \cdot E_{i,loc}$. Both the absorption and the scattering cross sections (C_{abs} and C_{sca}) can be directly obtained from P_i.

RESULTS AND DISCUSSION

The bar-shaped Au−Pd core−shell nanostructures are synthesized by a routine epitaxial growth templated on Au nanorods (Au NRs). Prepared through a seed-mediated method,[15] the Au NRs whose side surface is bounded by {100} and {110} facets have an average diameter of 16 nm and length of 66 nm with an aspect ratio of 4.1 (Figure S1). In the following epitaxial growth step, the focus of synthesis is to control the Pd shell thickness at atomic-level precision. Differently from the previous synthetic approaches,[16,17] we employ HCl together with O_2 in the air as etching agents to slow the reduction of Pd precursor (K_2PdCl_4) by ascorbic acid, which allows for the sustainable growth of Pd shells on Au NRs. By carefully varying the amounts of K_2PdCl_4 and ascorbic acid, the Pd shell thickness can be tuned from 2 to 27 layers (Figures 1 and S2−S5; denoted Au NRs−Pd_{2L} to Au NRs−Pd_{27L}). With cetyltrimethylammomium bromide (CTAB) as a capping agent to promote the formation of {100} facets, the oxidative etching by HCl and O_2 can remove the Pd atoms with higher surface energy so as to enlarge the coverage of {100} facets on surface.[18−21]

Figure 1 shows the transmission electron microscopy (TEM) analysis on the Au NRs−Pd_{2L} nanostructures with the thinnest Pd shells. As indicated by Figure 1a, the nanostructures inherit the rod-like shape from Au templates that possess an octagonal cross-section with a mix of {110} and {100} facets.[22] The high-resolution TEM (HRTEM) images in Figure 1b and c show the two orientations of the Au NRs−Pd_{2L} nanostructures. The lattice fringes can be well assigned to the {111} (Figure 1b) and {200} (Figure 1c) of face-center cubic (fcc) Au, respectively. This observation suggests that the sample after the Pd shell growth still remains a piece of single crystal with side faces bounded by {110} and {100} facets. To resolve the Pd shell thickness, the aberration-corrected high-angle annular dark-field scanning TEM (HAADF-STEM) is employed to characterize the samples. The HAADF-STEM images in Figure 1d and e show a high-brightness contrast in the core corresponding to Au and a low-brightness contrast corresponding to Pd. The location of Pd atoms is further verified by the HAADF-STEM images in which the Pd shell diminishes with increasing the contrast by prolonging exposure time on Au (Figure S2). Obviously, the shell is composed of two layers of Pd atoms. To confirm the core−shell structure, the elemental distributions of Pd and Au are characterized by the STEM and energy-dispersive spectroscopy (EDS) mapping analyses (Figure 1f), clearly revealing the coverage of Pd shell on Au NR.

By depositing more Pd atoms onto Au NRs, the core−shell nanocrystals are turned from rod-like to bar-like structures with a rectangular cross-section. As the {110} facets possess higher surface energy,[23] the {100} surface facets are enlarged at the expense of {110} with the assistance of capping agent CTAB. As indicated by the HRTEM images (Figures S3−S5), the resulting bar-like nanostructures are exclusively enclosed by {100} facets. The lattice fringes with a period of 2.0 Å can be well assigned to the {200} spacing of fcc Pd. On the basis of the contrast and the lattice constant, the shell thicknesses are determined to incrementally step up from 7 to 14 and then to 27 layers. The STEM and EDS mapping profiles further confirm the core−shell structures with Au cores and Pd shells. To examine the uniformity of shell thickness, we measure the molar ratios of Pd to Au in all of the samples by inductively coupled plasma mass spectrometry (ICP-MS, Figure S6 and Table S1), which turn out to be consistent with those calculated from the shell thickness determined by the TEM analyses.

The precise control over Pd shell thickness offers the flexibility for tailoring the plasmonic bands of Au NRs. In terms of the dielectric constant, Pd has a larger imaginary part than Au, and thus the addition of Pd layers would damp the plasmon resonance of Au NRs, enabling a fine-tuning of the plasmonic band position and intensity.[24] To examine the tunable plasmonic features, we collect the UV−vis extinction spectra for various Au NRs-based nanostructures (Figure S7), in combination with the discrete dipole approximation (DDA) calculations (Figure S8). The results clearly indicate that the Au NRs have two intrinsic plasmonic bands at 400−700 and 700−1000 nm, corresponding to the T and L modes, respectively, both of which are gradually blue-shifted and exhibit intensity reduction with increasing Pd layers. Remarkably, the plasmon damping by Pd dramatically broadens the extinction bandwidths, favoring the harvesting of photons to a large extent in full solar spectrum. Although the extinction band intensity maxima decrease with the Pd coating (Figure S7), the absorption coefficients associated with photothermal and hot electron effects are not much altered (Figure S8). This feature is due to the fact that Pd has a larger imaginary component of the dielectric constant, inducing the predominant absorption part in Pd-coated nanostructures.[14] Note that bare Au nanostructures do not possess catalytic activity despite their large extinction coefficients. The absorption dominating in the extinction cross sections, particularly when the Pd layers are thickened, would facilitate the implementation of local heating and plasmonic hot-electron effects in catalysis by minimizing the photon re-emission. As indicated by the calculated relative field amplitudes (Figure S9), optical near-field enhancement is concentrated on the Pd/Au surface and subsurface where the

DOI: 10.1021/jacs.6b02532
J. Am. Chem. Soc. 2016, 138, 6822−6828

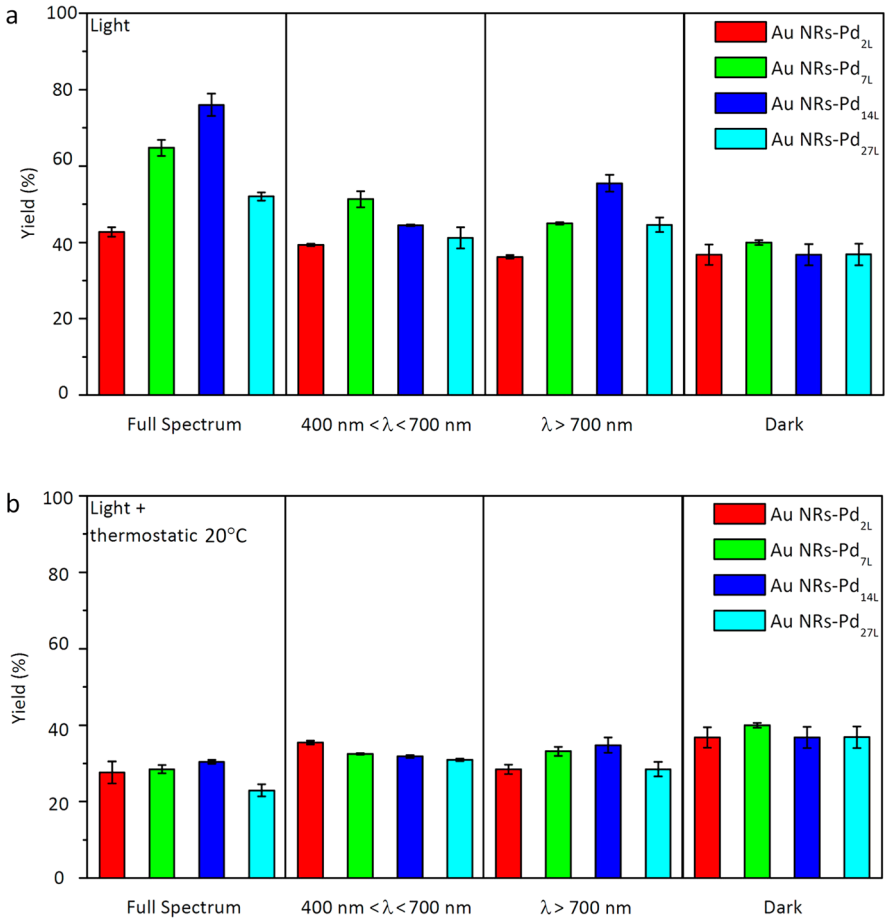

Figure 2. Catalytic performance of various Au NRs−Pd core−shell nanostructures in styrene hydrogenation under light irradiation. (a) Yield of ethylbenzene from the reaction without thermostatic control. The detailed data are listed in Table S2. (b) Yield of ethylbenzene from the reaction with thermostatic control at 20 ± 1 °C. The detailed data are listed in Table S3. Reaction conditions: 0.2 mmol of styrene and catalyst containing 0.145 mg of Au in 1 mL of H_2O, 1 atm 100% H_2, 1 h, no additional heating. The reaction performed in the dark at 20 ± 1 °C is used as a reference.

plasmonic hot electrons and local heat can be intensively generated and transferred to reactant molecules through the Pd layers.

Hydrogenation represents a large category of organic reactions commonly involved in various chemical processes, which can be efficiently catalyzed by Pd in a thermal process as Pd is well-known to strongly interact with molecular hydrogen (H_2).[5] In our design, the plasmonic Au templates underneath the Au NRs−Pd core−shell nanostructures can supply heat and hot electrons for catalytic hydrogenation on Pd surface. To assess the performance in light-driven reactions, we perform the hydrogenation of styrene using Au NRs−Pd core−shell nanostructures with varied Pd shell thicknesses under light illumination at room temperature (Figure 2a and Table S2). In full spectrum, the yield of ethylbenzene exhibits a volcano-shaped relationship with the Pd thickness. Apparently this performance dependence on Pd thickness is not caused by the alteration of intrinsic catalytic ability, as the catalytic hydrogenation performance in the dark at both 20 and 70 °C turns out to be constant regardless of Pd thickness variation (Figures 2a and S10). Strikingly, the Au NRs−Pd_{14L} nanostructures attain the highest conversion yield at 76% under the full-spectrum irradiation of 100 mW cm^{-2}, which turns out to be comparable to that achieved in the thermally driven process at 80 °C (see Figure S11). As the Au NRs−Pd core−shell nanostructures have two plasmonic bands (T mode at 400−700 nm and L mode at 700−1000 nm), we further interrogate the performance dependence on shell thickness in each specific mode by narrowing the irradiation spectra. Apparently, the volcano profiles distinguish between the T and L modes, peaking at Au NRs−Pd_{7L} and Au NRs−Pd_{14L}, respectively.

This finding, revealing the excellent light-driven performance, paves the way to optimize the design of plasmonic−catalytic materials through shell tailoring. Yet, in efforts to materialize the optimal design, a critical question cannot be circumvented: what factors cause such a volcano-shaped relationship? Intuitively, this question could be addressed if one can separately look into the contributions of photothermal and plasmonic hot-electron effects to the hydrogenation. To this end, the light-driven catalytic hydrogenation is carried out when the system temperature is maintained at 20 ± 1 °C using a thermostatic control device (Figure 2b and Table S3). As such, the effect of photothermal conversion on catalytic reaction would be suppressed to reduce the yield of ethylbenzene. For instance, the yield by Au NRs−Pd_{14L} in full spectrum is reduced from 76.0% to 30.4% with the thermostatic control. The reduced amount of yield (e.g., 45.6% for Au NRs−Pd_{14L} in full spectrum, Table 1) should be mainly ascribed to the contribution from local heating by photothermal conversion.[11,12]

Note that this thermostatic control is applied to both the reaction species and the plasmonic nanostructures that are

DOI: 10.1021/jacs.6b02532
J. Am. Chem. Soc. 2016, 138, 6822−6828

Table 1. Photothermal Contribution by Various Au NRs−Pd Core−Shell Nanostructures in Styrene Hydrogenation for Different Plasmonic Modes[a]

sample	full spectrum (%)	T mode (%)	L mode (%)
Au NRs−Pd_{2L}	15.1	3.8	7.7
Au NRs−Pd_{7L}	38.3	18.8	11.9
Au NRs−Pd_{14L}	45.6	12.7	20.8
Au NRs−Pd_{27L}	29.1	10.3	16.1

[a]T and L modes denote the performances under irradiation of 400 < λ < 700 nm and λ > 700 nm, respectively. The calculations are performed by subtracting the yield with thermostatic control at 20 °C (Table S3) from that without thermostatic control (Table S2).

surrounded by solution. In this system, the Pd surface of plasmonic nanostructures is cooled by the solution so as to reduce the plasmonic photothermal contribution to hydrogenation reactions. Certainly the efficiency of cooling plasmonic nanostructures by solution depends on the heat transfer from nanostructure surface to solution, in which initial solution temperature is the key parameter.[4,14,25] The catalytic hydrogenation performance under full-spectrum irradiation at various temperatures (Figure S12) reveals that the deviation of hydrogenation yields is very limited between 0−20 °C, indicating that the photothermal contribution to hydrogenation reactions has been largely eliminated within this temperature regime. As all of the light-irradiated hydrogenation reactions are carried out at the initial solution temperature of 20 °C (i.e., room temperature), we choose 20 °C for the thermostatic control to simplify the case. On the other hand, it is worth pointing out that the actual photothermal contribution to hydrogenation reactions should be slightly larger than that estimated through this method as the heating effect from Pd surface cannot be completely excluded. Nevertheless, this investigation can give a picture on the trend of thickness-dependent performance.

We also notice that eliminating the photothermal contribution (i.e., with the thermostatic control) can reduce the efficiency down below the control value in the dark (Table S3). Again, taking the full-spectrum performance of Au NRs−Pd_{14L} as an example, it is 6.3% lower than that at the same temperature in the dark. This light-induced performance decay is quite constant at each certain temperature between 0−20 °C (Figure S13). It is recognized that the supply of hot electrons to Pd surface disfavors Pd−H dissociation and reduces hydrogenation efficiency.[3,5] Thus, it is safe to attribute this light-induced performance decay at constant temperature (Table 2) to the detrimental effect from plasmonic hot electrons. As a small portion of photothermal contribution may still be involved in the thermostatic-control experiments, the detrimental effect from plasmonic hot electrons could be slightly larger than that estimated here. It is seen from the analyses in Tables 1 and 2 that both local heating and hot-electron transfer have a nontrivial dependence on Pd shell thickness, suggesting that we have a versatile knob at hand for maneuvering the two effects on catalytic reactions.

Table 2. Hot-Electron Contribution by Various Au NRs−Pd Core−Shell Nanostructures in Styrene Hydrogenation for Different Plasmonic Modes[a]

sample	full spectrum (%)	T mode (%)	L mode (%)
Au NRs−Pd_{2L}	−9.2	−1.3	−8.3
Au NRs−Pd_{7L}	−11.5	−7.5	−6.9
Au NRs−Pd_{14L}	−6.3	−4.9	−2.0
Au NRs−Pd_{27L}	−13.9	−5.9	−8.3

[a]T and L modes denote the performance under irradiation of 400 < λ < 700 nm and λ > 700 nm, respectively. The calculations are performed by subtracting the yield in the dark at 20 °C from that with thermostatic control at 20 °C (Table S3).

To decipher the mechanisms underlying such a nontrivial dependence, we attempt to capture the dynamics of surface plasmon decay with a focus on the electron−phonon scattering and charge recombination that account for the rate of generating local heat and the lifetime of plasmonic hot electrons, respectively. We resort to ultrafast transient absorption (TA) spectroscopy, a robust tool for tracking in real time the carrier dynamics involved in nanostructured systems,[14,26−28] to characterize the samples. Using a time-resolved, visible pump/white-light continuum (WLC) probe scheme spanning several nanoseconds with femtosecond resolution, we interrogate the Au NRs−Pd core−shell nanostructures with different Pd shell thicknesses to evaluate their performance in electron−phonon scattering and charge recombination, with the bare Au NRs as a reference sample (Figure S14).

We first examine the L mode located at 700−1000 nm. Figure 3a displays a set of representative temporally resolved

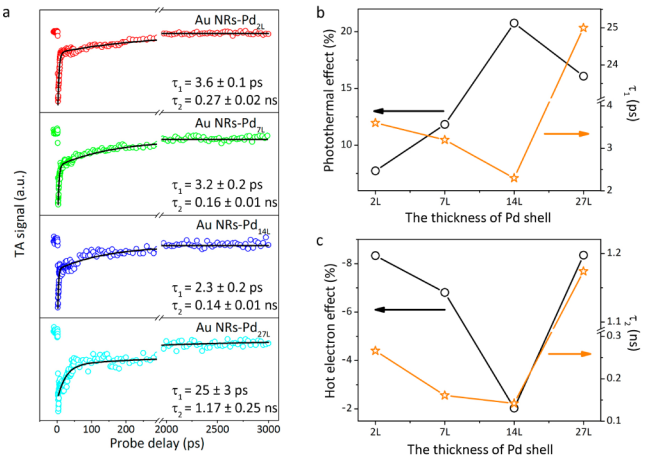

Figure 3. Ultrafast transient absorption spectroscopy characterization and evaluation of plasmonic contributions to hydrogenation by L mode. (a) TA signal as a function of probe delay for Au NRs−Pd core−shell nanostructures dispersed in water, recorded with a 650 nm pump and probed at 700 nm. τ_1, electron−phonon scattering; τ_2, charge recombination. (b) Photothermal effect on styrene hydrogenation under irradiation of λ > 700 nm (derived from the data in Table 1) in comparison with time constants for electron−phonon scattering. (c) Hot-electron effect on styrene hydrogenation under irradiation of λ > 700 nm (derived from the data in Table 2) in comparison with time constants responsible for charge recombination.

TA spectra taken at 700 nm, recorded with a 650 nm pump. Upon photoexcitation, the electrons in Au are promoted to the excited states, heating up the electrons. The increase in electron temperature induces a TA bleach due to the broadened plasmonic band,[14] reflecting the generation of plasmonic hot electrons and holes. Subsequently, the hot electrons undergo a series of heat exchange processes, including electron−phonon scattering and phonon−phonon scattering, to transfer the electron energy to phonon mode, levitating the lattice temperature near the Au surface. The fast exponential

DOI: 10.1021/jacs.6b02532
J. Am. Chem. Soc. 2016, 138, 6822−6828

relaxation on a time scale of a few picoseconds is attributed to the electron−phonon scattering process, whose time constant (τ_1) relates to the generation rate of local heat. The eventual recovery of the TA bleach on a longer time scale of hundreds of picoseconds is attributed to the charge recombination process,[28] whose time constant (τ_2) relates to the lifetime of hot electrons. Note that the phonon−phonon scattering process typically occurs on a time scale of tens of picoseconds, which cannot be separately resolved in the TA kinetic traces as it appears superimposed on the overall TA signal.

After acquiring the pertinent time constants, we are in a position to correlate them with the effects of local heating and plasmonic hot electrons on styrene hydrogenation. Figure 3b compares the time constants of electron−phonon scattering (τ_1) with the photothermal contributions, from which one can detect a nice correlation: faster generation of local heat induces stronger photothermal effect. Typically, the hot electrons generated in Au will come across the Au−Pd interface and enter the Pd lattice. By increasing the Pd shell thickness, the hot electrons tend to interact more thoroughly with the Pd lattice to generate heat for photothermal conversion. Nevertheless, if the Pd shells are too thick, hot electrons would be generated by the Pd shells on their own. It has been reported that the Pd shells with comparable wall thickness (5−6 nm) exhibit a broad plasmonic absorption band at 400−1000 nm, covering the visible and NIR region.[29,30] The Pd-generating hot electrons would undergo electron−phonon scattering relaxation to increase the temperature of Pd lattice, thereby reducing the heat capacity of Pd shells. This may slow the electron−phonon scattering relaxation of Au-generating hot electrons when they pass through the Pd shells.[14,27] As a result, the photothermal effect exhibits a volcano-shaped trend with a maximum at Au NRs−Pd_{14L}.

On the other hand, it is found that the time constants of charge recombination (τ_2) follow a similar relationship (Figure 3c). The thickening of the Pd shells lengthens the traveling path of hot electrons, facilitating charge recombination. The acceleration of charge recombination suppresses the side effect from hot electrons. Once the thickness reaches a threshold, the hot electrons generated by the Pd shells would come into play, prolonging the charge recombination time. Therefore, it is understandable that the Au NRs−Pd_{14L} sample stands out with the highest catalytic hydrogenation efficiency (under irradiation of 700−1000 nm) because its just-right thickness of Pd shell enables a perfect, synergistic combination of the maximal photothermal heating and the minimal detrimental effect from hot electrons. Note that the hot electrons should not participate in the reactions via charge transfer during the hydrogenation reactions. Instead, the electrons only enhance the binding of dissociated H atoms to Pd surface and reduce the efficiency of hydrogenation reactions.[5,31] As such, the hot electrons that are not consumed in the reactions would eventually recombine with the hot holes.

It is natural to ask whether the T mode falls into the same situation as the L mode. As the T mode is located at 400−700 nm, we choose a 480 nm pump as the photoexcitation source and monitor the TA kinetics at 520 nm. As shown in Figure 4a, apart from a similar existence of two processes of TA decay (τ_1 and τ_3), the major difference lies in the emergence of an additional, in-between process of TA growth on a time scale of tens of picoseconds (τ_2). This growing TA signal can be mainly attributed to the charge separation process.[28] This feature can be resolved most likely because the traveling length for T mode

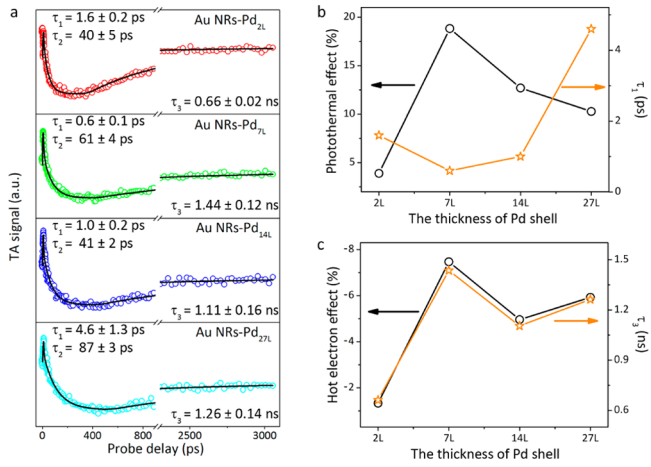

Figure 4. Ultrafast transient absorption spectroscopy characterization and evaluation of plasmonic contributions to hydrogenation by T mode. (a) TA signal as a function of probe delay for Au NRs−Pd core−shell nanostructures dispersed in water, recorded with a 480 nm pump and probed at 520 nm. τ_1, electron−phonon scattering; τ_2, charge separation; τ_3, charge recombination. (b) Photothermal effect on styrene hydrogenation under irradiation of $400 < \lambda < 700$ nm (derived from the data in Table 1) in comparison with time constants for electron−phonon scattering. (c) Hot-electron effect on styrene hydrogenation under irradiation of $400 < \lambda < 700$ nm (derived from the data in Table 2) in comparison with time constants responsible for charge recombination.

(~16 nm) is shorter than the mean free path in Au (~50 nm).[32] More importantly, the τ_1 and τ_3 time constants responsible for electron−phonon scattering and charge recombination, respectively, are also well resolved and deduced, providing references for performance assessment. Again, the dependences of τ_1 and τ_3 on Pd shell thickness exhibit nice correlation with the effects of local heating and plasmonic hot electrons on hydrogenation (Figure 4b and c).

Differently from the case of L mode, two features can be identified for T mode. First, the shorter traveling length favors the charge separation process, and thus the transport of hot electrons across the Au−Pd interface can be sensitively affected by interfacial quality. Note also that the inevitable lattice distortion by interfacial strain upon shrinking the Pd shell down to 2 layers would dramatically reduce the lifetime of hot electrons. Second, the electron−phonon scattering process exhibits the shortest time constant at the Pd shell thickness of 7 layers rather than 14 layers, most likely because the electron−phonon scattering relaxation along the short axis is faster. As a result, the Au NRs−Pd_{7L} sample achieves the best performance in styrene hydrogenation.

Overall, the correlations revealed above demonstrate that the variation in charge kinetics is strikingly consistent with the trend of hydrogenation yields. Both photothermal conversion and hot-electron generation can be subtly controlled to impact on catalytic reactions by altering shell thickness. The structure−plasmon−catalysis interplay understood in this work thus provides new opportunities for better harnessing surface plasmon decay toward optimized catalytic performance.

CONCLUSION

We have developed a series of Au NRs−Pd core−shell nanostructures with T and L plasmonic modes covering a broad spectrum from 400 to 1000 nm. The developed

DOI: 10.1021/jacs.6b02532
J. Am. Chem. Soc. 2016, 138, 6822−6828

nanostructures enable extensive harvesting of solar energy for catalytic reactions. More importantly, our synthetic protocol allows for controlling the shell thickness at atomic-level precision. As revealed by ultrafast absorption spectroscopy, the surface plasmon decay in nanostructures can be readily maneuvered through such precise controllability in synthesis. It offers tunable behaviors in local-heat generation and hot-electron transfer, setting up an excellent platform for correlating the two plasmonic effects with catalytic performance. The perfect consistency discovered in this work clearly demonstrates that the photothermal and hot-electron effects can be separately manipulated through delicate materials design to maximize the catalytic efficiency driven by visible−NIR light. Despite the detrimental effect of hot electrons on hydrogenation, the information gleaned here would provide valuable guidance in the materials design for other types of reactions in which the plasmonic hot electrons can make positive contributions. In that case, synergistic interplay of local-heat generation and hot-electron transfer may enhance the reactions beyond the capability of conventional thermal-driven reactions. This work opens a new avenue for rationally developing plasmonic−catalytic nanostructures toward efficient solar-to-chemical energy conversion.

■ ASSOCIATED CONTENT

Supporting Information

The Supporting Information is available free of charge on the ACS Publications website at DOI: 10.1021/jacs.6b02532.

Detailed experimental section, characterization methods, and additional material characterizations (PDF)

■ AUTHOR INFORMATION

Corresponding Authors

*qunzh@ustc.edu.cn

*yjxiong@ustc.edu.cn

Author Contributions

‖H.H. and L.Z. contributed equally to this work.

Notes

The authors declare no competing financial interest.

■ ACKNOWLEDGMENTS

We acknowledge financial support from the NSFC (nos. 21471141, 21573211, 21421063, 11434017), the Recruitment Program of Global Experts, the CAS Hundred Talent Program, the Hefei Science Center of the CAS (nos. 2015HSC-UP009, 2015HSC-UE008), the Strategic Priority Research Program of the CAS (XDB01020000), and the Fundamental Research Funds for the Central Universities (nos. WK2060190025, WK2340000063).

■ REFERENCES

(1) Linic, S.; Aslam, U.; Boerigter, C.; Morabito, M. *Nat. Mater.* **2015**, *14*, 567−576.

(2) Baffou, G.; Quidant, R. *Chem. Soc. Rev.* **2014**, *43*, 3898−3907.

(3) Long, R.; Li, Y.; Song, L.; Xiong, Y. *Small* **2015**, *11*, 3873−3889.

(4) Wang, F.; Li, C.; Chen, H.; Jiang, R.; Sun, L. D.; Li, Q.; Wang, J.; Yu, J. C.; Yan, C. H. *J. Am. Chem. Soc.* **2013**, *135*, 5588−5601.

(5) Long, R.; Rao, Z.; Mao, K.; Li, Y.; Zhang, C.; Liu, Q.; Wang, C.; Li, Z. Y.; Wu, X.; Xiong, Y. *Angew. Chem., Int. Ed.* **2015**, *54*, 2425−2430.

(6) Huang, X.; Li, Y.; Chen, Y.; Zhou, H.; Duan, X.; Huang, Y. *Angew. Chem., Int. Ed.* **2013**, *52*, 6063−6067.

(7) Brongersma, M. L.; Halas, N. J.; Nordlander, P. *Nat. Nanotechnol.* **2015**, *10*, 25−34.

(8) Christopher, P.; Xin, H.; Linic, S. *Nat. Chem.* **2011**, *3*, 467−472.

(9) Christopher, P.; Xin, H.; Marimuthu, A.; Linic, S. *Nat. Mater.* **2012**, *11*, 1044−1050.

(10) Sarina, S.; Zhu, H.; Jaatinen, E.; Xiao, Q.; Liu, H.; Jia, J.; Chen, C.; Zhao, J. *J. Am. Chem. Soc.* **2013**, *135*, 5793−5801.

(11) Zheng, Z.; Tachikawa, T.; Majima, T. *J. Am. Chem. Soc.* **2015**, *137*, 948−957.

(12) Zheng, Z.; Tachikawa, T.; Majima, T. *J. Am. Chem. Soc.* **2014**, *136*, 6870−6873.

(13) Xia, Y.; Halas, N. J. *MRS Bull.* **2005**, *30*, 338−343.

(14) Hartland, G. V. *Chem. Rev.* **2011**, *111*, 3858−3887.

(15) Nikoobakht, B.; El-Sayed, M. A. *Chem. Mater.* **2003**, *15*, 1957−1952.

(16) Xiang, Y.; Wu, X.; Liu, D.; Jiang, X.; Chu, W.; Li, Z.; Ma, Y.; Zhou, W.; Xia, S. *Nano Lett.* **2006**, *6*, 2290−2294.

(17) Zhang, K.; Xiang, Y.; Wu, X.; Feng, L.; He, W.; Liu, J.; Zhou, W.; Xie, S. *Langmuir* **2009**, *25*, 1162−1168.

(18) Long, R.; Zhou, S.; Wiley, B. J.; Xiong, Y. *Chem. Soc. Rev.* **2014**, *43*, 6288−6310.

(19) Li, B.; Long, R.; Zhong, X.; Bai, Y.; Zhu, Z.; Zhang, X.; Zhi, M.; He, J.; Wang, C.; Li, Z. Y.; Xiong, Y. *Small* **2012**, *8*, 1710−1716.

(20) Personick, M. L.; Mirkin, C. A. *J. Am. Chem. Soc.* **2013**, *135*, 18238−18247.

(21) Yang, Y.; Liu, J.; Fu, Z. W.; Qin, D. *J. Am. Chem. Soc.* **2014**, *136*, 8153−8156.

(22) Xiong, Y.; Cai, H.; Wiley, B. J.; Wang, J.; Kim, M.; Xia, Y. *J. Am. Chem. Soc.* **2007**, *129*, 3665−3675.

(23) Xia, Y.; Xiong, Y.; Lim, B.; Skrabalak, S. E. *Angew. Chem., Int. Ed.* **2009**, *48*, 60−109.

(24) Zhang, C.; Chen, B.-Q.; Li, Z.-Y.; Xia, Y.; Chen, Y.-G. *J. Phys. Chem. C* **2015**, *119*, 16836−16845.

(25) Hogan, N. J.; Urban, A. S.; Ayala-Orozco, C.; Pimpinelli, A.; Nordlander, P.; Halas, N. J. *Nano Lett.* **2014**, *14*, 4640−4645.

(26) *Femtosecond Laser Spectroscopy*; Hannaford, P., Ed.; Springer: New York, 2005.

(27) Yu, K.; Polavarapu, L.; Xu, Q. H. *J. Phys. Chem. A* **2011**, *115*, 3820−3826.

(28) Zhao, T.; Jiang, X. F.; Gao, N.; Li, S.; Zhou, N.; Ma, R.; Xu, Q. H. *J. Phys. Chem. B* **2013**, *117*, 15576−15583.

(29) Xiong, Y.; Wiley, B.; Chen, J.; Li, Z.-Y.; Yin, Y.; Xia, Y. *Angew. Chem., Int. Ed.* **2005**, *44*, 7913−7917.

(30) Chen, J.; Wiley, B.; McLellan, J. M.; Xiong, Y.; Li, Z.-Y.; Xia, Y. *Nano Lett.* **2005**, *5*, 2058−2062.

(31) Kyriakou, G.; Boucher, M. B.; Jewell, A. D.; Lewis, E. A.; Lawton, T. J.; Baber, A. E.; Tierney, H. L.; Flytzani-Stephanopoulos, M.; Sykes, E. C. H. *Science* **2012**, *335*, 1209−1212.

(32) Link, S.; El-Sayed, M. A. *J. Phys. Chem. B* **1999**, *103*, 4212−4217.

DOI: 10.1021/jacs.6b02532
J. Am. Chem. Soc. 2016, 138, 6822−6828